



Contents lists available at ScienceDirect

Engineering Fracture Mechanics

journal homepage: www.elsevier.com/locate/engfracmech

Fracture mechanics analyses of a reactor pressure vessel under non-uniform cooling with a combined TRACE-XFEM approach

D.F. Mora^{a,*}, O. Costa Garrido^{a,b}, R. Mukin^c, M. Niffenegger^a^a Paul Scherrer Institut, Nuclear Energy and Safety Department, Structural Integrity Group, CH-5232 Villigen PSI, Switzerland^b Jožef Stefan Institute, Jamova cesta 39, SI-1000 Ljubljana, Slovenia^c Paul Scherrer Institut, Nuclear Energy and Safety Department, Laboratory for Reactor Physics and Thermal-Hydraulics, CH-5232 Villigen PSI, Switzerland

ARTICLE INFO

Keywords:

Pressurized thermal shock
 Loss-of-coolant accident
 Stress intensity factor
 Reactor pressure vessel
 Fracture mechanics
 Extended finite element method (XFEM)

ABSTRACT

This paper presents the integrity analyses of a model reactor pressure vessel (RPV) subjected to pressurized thermal shocks (PTS). The analyses are performed with a one-way multi-step strategy that includes the thermo-hydraulics, thermo-mechanical and fracture mechanics analyses to simulate three hypothetical loss of coolant accidents (LOCA). The thermo-hydraulics analyses are performed with the system code TRACE and a three-dimensional (3D) model of the RPV, providing the input for the structural analyses with the finite element code ABAQUS. These employ a sequential use of global model (entire RPV) and submodels (a portion of the RPV containing the crack), where the eXtended Finite Element (XFEM) approach is employed to compute the stress intensity factor (SIF) of a postulated crack in the RPV wall.

The results first present a verification of the multi-step strategy with the FAVOR code for uniform temperature distribution in the RPV wall. Under uniform temperature and pressure load, a significant effect of the nozzle geometry on the asymmetric stress distribution is demonstrated. The second part of the results shows that the stresses and the SIFs are also sensitive to the non-uniform temperatures due to the presence of the cooling plumes. It is also confirmed that the analyses with ABAQUS and FAVOR provide very similar results for the medium and large break LOCA transients. For the small break LOCA, the FAVOR code underestimates the SIFs due to the missing nozzle geometry in combination with system pressure. Finally, the paper corroborates that the use of TRACE and XFEM, within the one-way multi-step simulation strategy, reduces the computational costs and the number of assumptions and approximations needed for feasible and reliable 3D fracture mechanics analyses of the RPV with consideration of the cooling plume effect.

1. Introduction

In nuclear power plants, the structural integrity of the reactor pressure vessel (RPV) has to be assured in normal and accident conditions. In the absence of radiation damage, the favorable fracture toughness of the RPV material ensures that there is no risk of failure in all operating conditions. This scenario changes substantially with time as the RPV is subjected to intensive neutron irradiation leading to embrittlement [1,2]. In accident scenarios with drastic temperature and pressure changes, the load concentration at defects will substantially increase the chances of crack initiation and propagation [3,4]. A critical accident scenario for the RPV is a

* Corresponding author. Tel.: +41563104364.

E-mail address: diego.mora@psi.ch (D.F. Mora).

<https://doi.org/10.1016/j.engfracmech.2020.107258>

Received 4 May 2020; Received in revised form 6 July 2020; Accepted 5 August 2020

Available online 14 August 2020

0013-7944/ © 2020 The Authors. Published by Elsevier Ltd.

Nomenclature			
1D, 3D	one and three dimensional	r_i, r_o	inner and outer radii of the RPV [m]
BC	boundary condition	r	radial coordinate [m]
CAD	computer aided design	th	wall thickness of the RPV [m]
CFD	computational fluid dynamics	J	J -Integral [MPa·m]
CL	cold leg	J_{int}^α	interaction integral
DC	downcomer	J_{int}^α	interaction integral for a virtual crack advance
ECC	emergency core cooling	\mathbf{I}	second order identity tensor
FEM	finite element method	\mathbf{u}	nodal displacement vector
HL	hot leg	\mathbf{x}	element coordinate vector
LBLOCA	large break loss-of-coolant accident	\mathbf{K}	vector of stress intensity factors
MBLOCA	medium break loss-of-coolant accident	\mathbf{n}	outward normal to the surface enclosing the crack tip
PTS	pressurized thermal shock	L	crack front
RPV	reactor pressure vessel	P	node set along the crack front line
SBLOCA	small break loss-of-coolant accident	\mathbf{q}	local direction of the virtual crack propagation.
SIF	stress intensity factor	T	temperature [°C]
USNRC	United States nuclear regulatory commission	s	position of a point at the crack front
XFEM	eXtended Finite Element Method	S_M	Von Mises stress [MPa]
a	crack depth [m]	u_i, u_i^{aux}	displacement and auxiliary displacement components [m]
C_p, K^*_j	coefficients of the polynomial approximation of the stress	u_{XFEM}	displacement field for XFEM
ct	crack tip	t	time [min]
$2c$	crack length [m]	Z	axial coordinate
dA	surface element of the tubular surface enclosing the crack tip	α	auxiliary mode of failure
E	elastic modulus [Pa]	ν	Poisson ratio
G	shear modulus [Pa]	θ	azimuthal coordinate
$F_\alpha(\mathbf{x})$	crack tip functions	$\lambda(s)$	virtual crack advance
\mathbf{K}	vector of stress intensity factor	$\boldsymbol{\varepsilon}, \boldsymbol{\varepsilon}_{aux}^\alpha$	strain and auxiliary strain tensor
K_I	Mode I linear elastic stress intensity factor [MPa·m ^{0.5}]	$\boldsymbol{\sigma}, \boldsymbol{\sigma}_{aux}^\alpha$	stress and auxiliary stress tensor [MPa]
K_{IC}	material fracture toughness [MPa·m ^{0.5}]	σ_n	normal stress to the crack plane [MPa]
RT_{NDT}	Nil-ductility transition reference temperature [°C]	$\sigma: \boldsymbol{\varepsilon}$	double contraction of second order tensors
		$\boldsymbol{\sigma} \cdot \mathbf{u}$	single contraction of second order tensor and vector

pressurized thermal shock (PTS), which is characterized by the rapid cooling of wall sections due to the injection of cold emergency coolant during a loss of coolant accident (LOCA) [5]. Thus, fracture mechanic analyses of the RPV under PTS loads represent an essential cornerstone in the assessment of lifetime extension of currently operating nuclear power plants near the end of their design life.

Structural integrity analyses of the RPV subjected to PTS have been the objective of several cooperative programs in the past and involve thermo-hydraulics, thermo-mechanical and fracture mechanics disciplines [6]. The analysis is typically performed with a series of sequential steps coupling different computer codes [7,8]. The diagram in Fig. 1 sketches the one-way multi-step simulation strategy often applied in the integrity assessment of the RPV. The definition of the hypothetical loss of coolant accident is assigned as Step 0. Then, given a PTS scenario, the first step of the calculation is the thermo-hydraulic (TH) analysis (step 1), the results of which are the thermal and pressure loads affecting the RPV [9]. The next steps are the thermo-mechanical and fracture mechanics analyses indicated as step 2 and 3, respectively, in Fig. 1.

The TH analyses are performed with the so-called system codes to simulate the entire reactor system during the accident and anticipate the transient conditions of the RPV [10]. Systems codes such as RELAP (Reactor Excursion and Leak Analysis and Program [11]) or TRACE (TRAC/RELAP Advanced Computational Engine [12]) solve the fluid governing equations based on assumptions that disregard the fluid dynamics complexity. Examples of the RPV integrity studies using RELAP results can be found in Refs [3,4,13,14]. To improve the prediction of local phenomena in the RPV, such as the cooling plume effects, previous studies [5,15–17] have presented a sequential analysis that uses the RELAP results as boundary conditions for the subsequent computational fluid dynamics (CFD) simulation of the RPV. While the use of advanced CFD simulations clearly allows studying the fluid transient inside the RPV in detail, they are still under development and suffer from very long computational times [18,19]. An alternative is e.g. the use of the three-dimensional (3D) capabilities recently developed into the system code TRACE. A 3D model of the RPV with TRACE have been already used in the screening analyses of PTS scenarios showing a good agreement with CFD simulations for high flow rates [20,21]. The preliminary output from TRACE for one PTS transient of short duration (~1000 s) has recently delivered promising results for its potential use in structural analyses of RPVs [22]. The RELAP, CFD and preliminary TRACE outputs have also been employed to analyze the variability in the integrity analysis from the use of different numerical tools [23].

When the output from the TH analysis is available, two approaches are typically used in practice to perform the thermo-

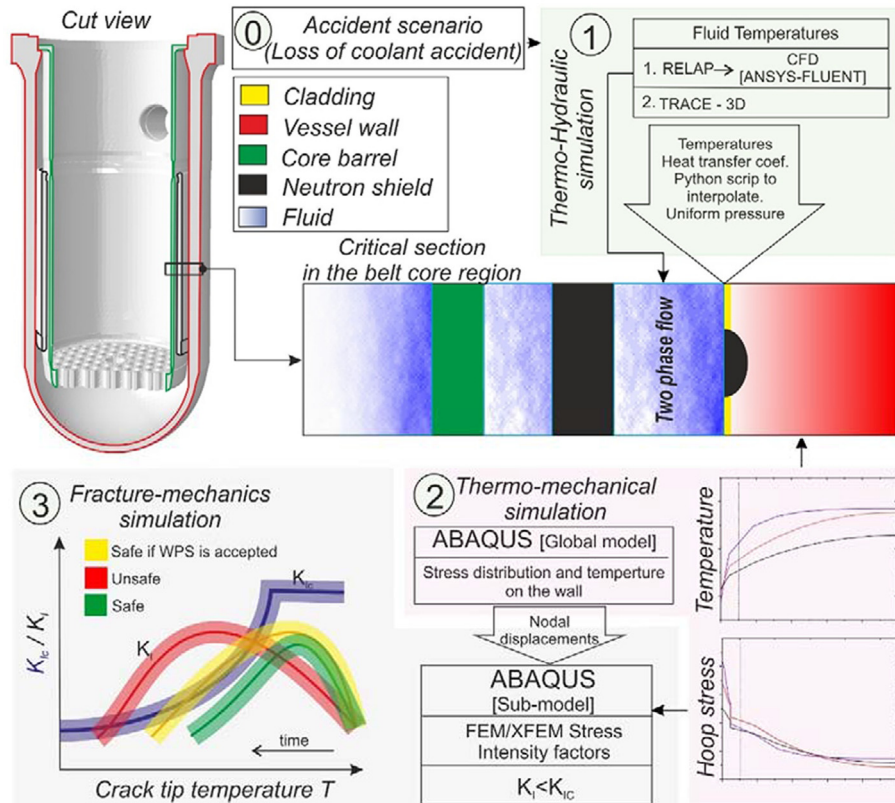


Fig. 1. One-way multi-step simulation strategy for the integrity analysis of a reactor pressure vessel subjected to pressurized thermal shock.

mechanical and fracture mechanics analyses; namely those that employ one- (1D) and three-dimensional (3D) computational models of the RPV. The advantage of the 1D model is that it is fast and reliable. On the other hand, it omits the RPV geometrical details by assuming a cylindrical shape and where the heat fluxes occur only in the radial (through-thickness) direction. The 1D model is nevertheless used in well-known computer codes such as FAVOR “Fracture Analysis of Vessels: Oak Bridge” code [24]. The 3D models, presented in the second and third steps in the multi-step strategy in Fig. 1, employ the global model and submodels of the RPV sequentially (step 2). The stresses are calculated in the global finite element model (FEM) and the submodeling technique is used to calculate the stress intensity factor (SIF) of postulated cracks in the RPV wall [15]. The evaluation of the SIF by the classical FE method requires a refinement and adaptation of the mesh around the crack tip [14,16]. The submodels in the multi-step strategy in Fig. 1, however, use the eXtended FEM (XFEM) approach. The main advantage of XFEM is the mesh independence on the discontinuity. Thus, its strength lies in the less stringent meshes around the crack tip, making it computationally more affordable for long transient simulations and especially to avoid remeshing in crack growth analyses. The RPV integrity analyses using 1D and 3D models, respectively, with FAVOR and XFEM tools have been presented in the literature [3,5,22,23]. However, the result’s discrepancies between both approaches were not studied in detail.

In this paper, the results of TRACE 3D simulations for three PTS scenarios are used together with the FE global model and submodels using XFEM to perform fracture mechanics analyses. In this contribution, a longer version of PTS transient presented in [22,23] and two additional PTS scenarios are considered. The SIF computed for a postulated surface crack in the RPV wall is then used to evaluate the likelihood of brittle crack propagation during the selected loss of coolant accidents. The thermo-hydraulic simulations are briefly described in Section 2 and Section 3 presents the modeling approaches and computational tools used to perform the thermo-mechanical and fracture mechanics analyses of the RPV. With the aim to verify the multi-step simulation strategy in Fig. 1, Section 4 presents in the first place the results of the integrity analysis for a uniform temperature distribution of the interior of the RPV with the ABAQUS code [25] and this is compared in detail with results of the FAVOR code. The effects of thermal diffusivity and nozzles geometry on the computed stresses and SIFs are thus demonstrated. These findings are then used to understand the second part of the results in Section 4, where the fracture mechanics analyses of the selected transients are performed using the non-uniform thermo-hydraulic output from TRACE. Finally, the conclusions are drawn in Section 5.

The work presented in this paper represents the first attempt to employ the 3D capabilities of TRACE to illustrate the non-uniform cooling effects in the integrity analysis of the RPV for three different and long PTS transient scenarios. To the authors’ knowledge, the results show for the first time how the stress fields and SIF values are affected by the geometric irregularities of the RPV, which was omitted in previous studies. This improves the understanding of the differences between 1D and 3D models of the RPV, thus verifying the strategy and corroborating the use of TRACE and XFEM for feasible and reliable 3D fracture mechanics analyses of the RPV with

consideration of the cooling plume effect.

2. Thermo-hydraulic simulation of loss of coolant accidents

In Mukin et al. [20], the transients following a full spectrum of break sizes in the main reactor coolant lines, from a small break size of 2% of the pipe's cross sectional area to a double-ended guillotine break, were analyzed with the system code TRACE [26]. In order to make the comparison for different LOCAs, the present study is restricted to the three cases listed in Table 1, namely, a 3 cm² small break (SBLOCA), a 70 cm² medium break (MBLOCA) and a 3832 cm² large break (LBLOCA).

2.1. TRACE-3D model and assumptions

The system code TRACE was developed by the United States Nuclear Regulatory Commission (USNRC) to perform best-estimate analyses of operational and accident transient scenarios such as LOCA [26]. It is based on mass, momentum and energy conservation equations for the liquid and vapor phases. This code has been qualified to analyze large and small break LOCA in conventional pressurized water reactors (PWR). The results predicted by system codes like TRACE are known to be affected by different sources of errors, such as model deficiencies, approximations in the numerical solutions, nodalization effects and uncertainties in the boundary and initial conditions [10]. However, system codes have shown noticeable progress in their capabilities and have reached an acceptable level of maturity. The main advantages of using TRACE for PTS studies are the rather limited computational resources and time needed to perform simulations of complex and long transient scenarios, as well as the 3D modeling capabilities for the RPV. Therefore, one aim of this contribution is to use the results of state-of-the-art TH simulations with TRACE in the integrity analyses of the RPV under the selected LOCA scenarios.

The model of the RPV defined in TRACE is shown in Fig. 2 and its nodalization in Fig. 2(a). The 3D model of the downcomer (DC) and the lower plenum (LP) is considered here to capture important phenomena during the PTS transient, such as the multi-dimensional spreading and redistribution of the cold water plume, and the mixing as the flow enters from the DC to LP, where it turns from horizontal to vertical. These features cannot be predicted in the 1D multi-pipe-component of TRACE and RELAP [15,27]. The decomposition of the DC and LP into control volumes is done using a computer-aided design (CAD) model shown in Fig. 2(b). As it is shown in Fig. 2(b) and (c), the RPV is subdivided in 15 axial, 5 radial and 12 azimuthal physical volumes or "cells".

At the beginning of the considered transients, the reactor is assumed at normal operating conditions before the break occurs with a temperature of about 280 °C and 15.5 MPa system pressure. For all transients, the loss of offsite power following a turbine trip is also assumed, and all safety injection pumps and accumulators are available. The hot full power conditions at 102% with 108% decay heat and reactor trip based on the second SCRAM signal are also considered. The minimum temperature in the downcomer depends on the emergency core cooling (ECC) water temperature injected during the accident. A conservative assumption in PTS analyses is that the ECC water temperature is 10 °C.

2.2. Results of the thermo-hydraulic analyses

Out of all the available results from the TH analyses with TRACE, only the temperatures of the RPV inner surface and the fluid pressure are used in the structural analyses. It is worth to note here that, alternatively, the fluid temperature and the heat transfer coefficient could have been used instead. By using the RPV inner surface temperature, the convection boundary condition can be avoided in the subsequent thermo-mechanical analyses, as this has been already considered in the TH analyses with TRACE.

The pressure histories during the SB-, MB- and LBLOCA transients are presented in Fig. 3. Note that the pressure is uniform on the entire inner surface of the RPV, as the pressure difference due to the height of the water column is negligible.

Fig. 4 shows the temperature distribution of the RPV inner surface at different times during the SB-, MB- and LBLOCA transients. The temperature varies in the range of 10° to 280 °C, equivalent to the ECC water injection temperature and the initial temperature of the RPV, respectively. According to these results, one general observation is that the cooling plume in TRACE is vertical and remains below the inlet nozzle in the transients considered. This is to be expected as TRACE uses one-dimensional momentum equations for the pipe components. Therefore, the detailed effects observed in CFD simulations [18,17], such as the possible bending of the ECC water injection and, therefore, of the cooling plume, due to the nozzle bend cannot be captured by TRACE. These inertial effects depend on the actual flow rate of injected water and can effectively deviate the cooling plume from the centerline below the nozzle. Another effect that cannot be captured with TRACE is the oscillation of the cooling plume as a result of the interaction between the two plumes flowing down from opposite inlet nozzles [28]. Despite the fact that there may be a lack of accuracy in capturing the cooling plume in TRACE, the latest studies on accident scenarios have shown that a similar evolution of the minimum temperature of

Table 1
Definition of selected LOCA cases.

	Break position	Break size [cm ²]	Simulated time [s]
SBLOCA	Hot leg	3	27,000
MBLOCA	Hot leg	70	7000
LBLOCA	Hot leg	3832	2000

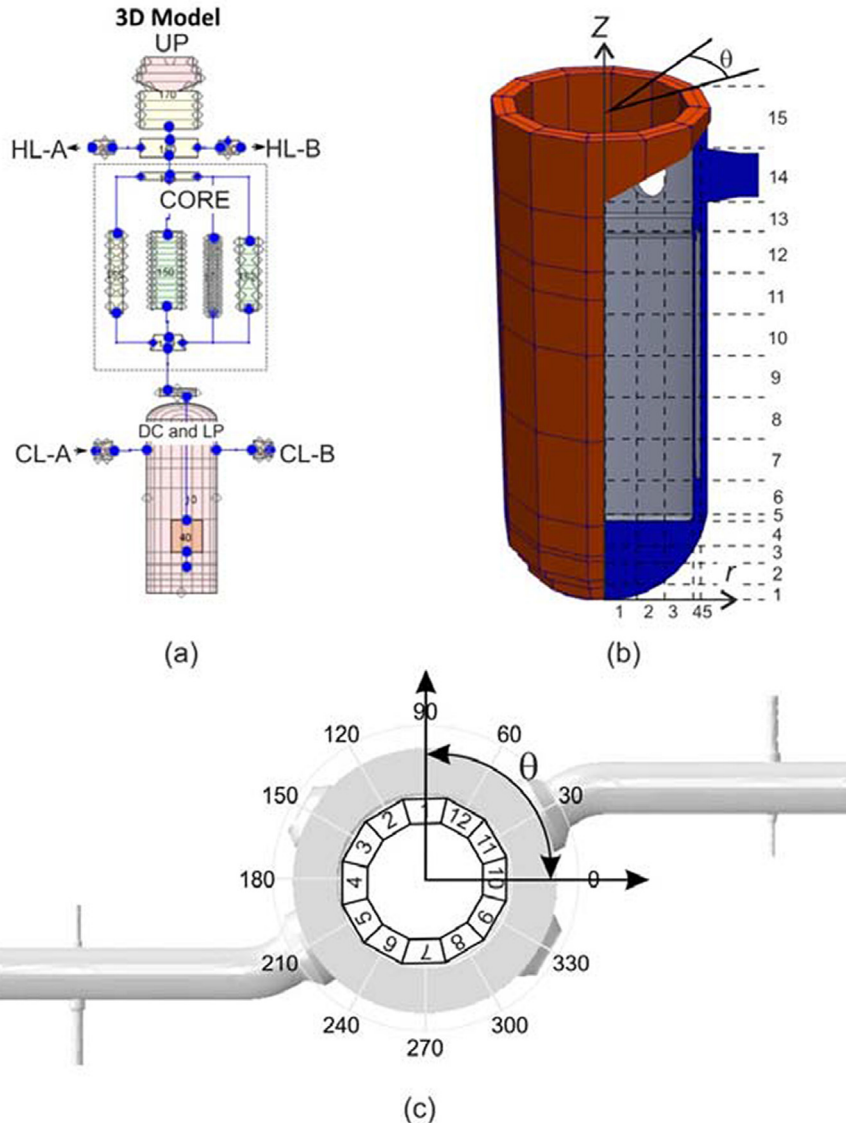


Fig. 2. Three-dimensional model of the RPV. (a) TRACE model nodalization of the RPV downcomer and lower plenum (UP: upper plenum, HL: hot leg, CL: cold leg), (b) CAD model of TRACE nodalization. The mesh of cells is defined in the cylindrical coordinates ($r - \theta - z$). (c) Upper view of the RPV with superimposed azimuthal (θ) nodalization.

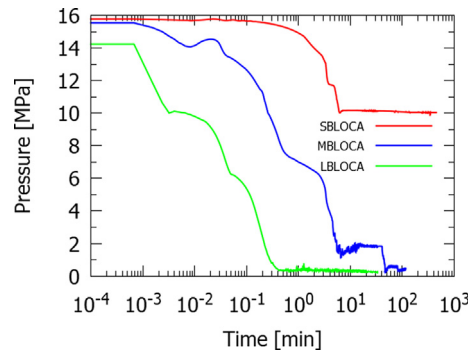


Fig. 3. Pressure histories during SB-, MB- and LBLOCA transients.

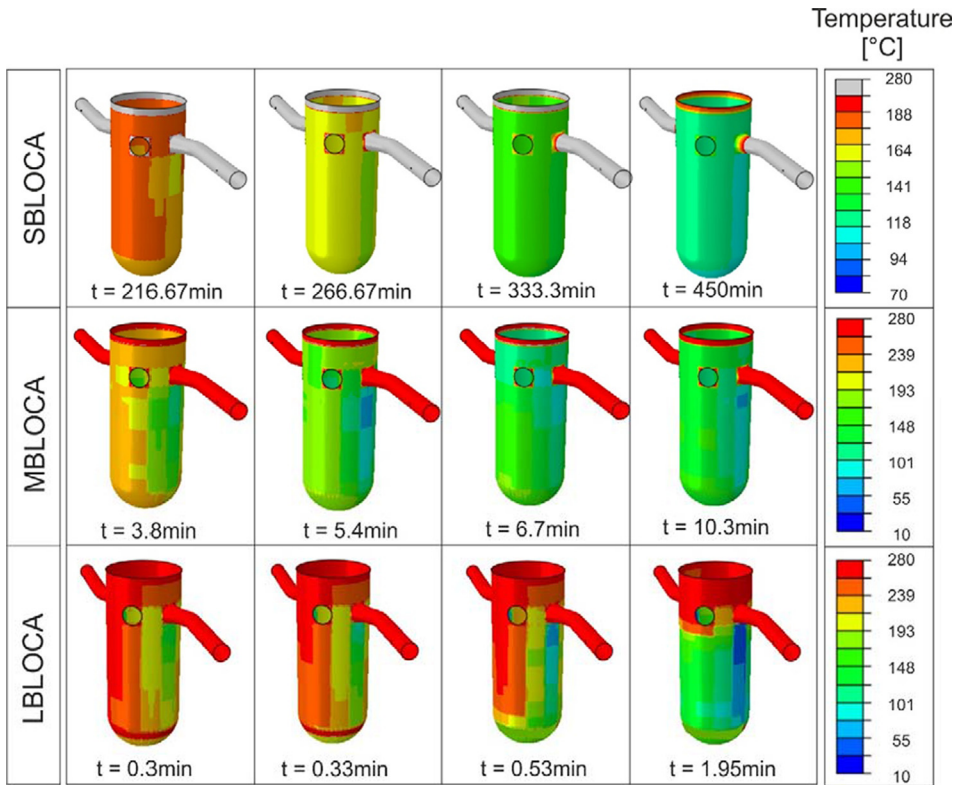


Fig. 4. Temperature distribution of the RPV inner surface during SB-, MB- and LBLOCA transients for different times t .

the DC wall is obtained with TRACE and CFD approaches [21].

Fig. 5 shows the temperature histories at the cell coordinate $(\theta, z) = (5 \text{ or } 210^\circ, 9)$ of the RPV inner surface (see Fig. 2) for the three LOCA scenarios considered. Note that this location is approximately in the middle of the core height and below the RPV nozzle where the ECC water is injected and, thus, within the cooling plume. As it can be expected, the results in Figs. 3 and 5 show that the bigger is the break size, the faster are the system depressurization and the temperature drop of the inner surface. Another interesting detail in Fig. 5 is the sudden increase of temperature in the LBLOCA curve at about 1 min into the transient. This is ascribed to the emptying of the accumulators.

The results of the thermo-hydraulic analyses just presented are employed as inputs in the subsequent thermo-mechanical analyses following two modeling approaches with 3D and 1D models of the RPV.

3. Modeling approaches for the RPV integrity analyses

This section describes the codes, models and assumptions used for the thermo-mechanical and fracture mechanics analyses of the RPV. Two approaches with 3D and 1D models of the RPV are presented, aiming at comparing and verifying their results.

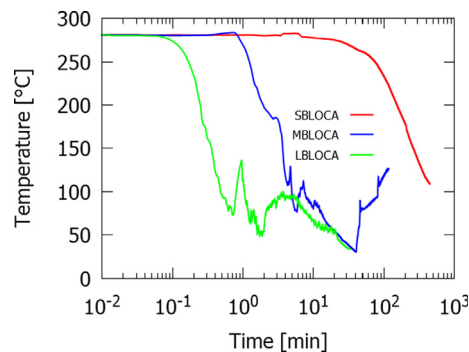


Fig. 5. Temperature histories of the inner surface of the RPV at the cell coordinate $(\theta - z) = (5, 9)$ in Fig. 2 during SB-, MB- and LBLOCA transients.

3.1. Three-dimensional analyses: code, models and assumptions

The ABAQUS finite element code [25] is used to develop the structural model of the RPV and to perform the thermo-mechanical and fracture mechanics analyses. The heat transfer (diffusion) analyses employ the 3D temperature distributions of the RPV inner surface shown in Fig. 4 as boundary conditions in order to obtain the time-dependent temperatures in the RPV wall. Fig. 6 presents the global model of the reference two-loop RPV and the mesh used for both, heat transfer and the subsequent mechanical, analyses. The RPV wall temperatures obtained in the heat transfer analyses together with the fluid pressure in Fig. 3 are used as inputs in the mechanical analyses. The calculation is performed assuming adiabatic boundary conditions at the outer RPV surface. In the mechanical analyses, the boundary conditions shown in Fig. 6left are used to allow free-deformation of the RPV while avoiding free-body motion. The global model mesh consists of 20-node quadratic bricks with reduced integration (C3D20R) elements. This mesh has been verified against the FAVOR results under the assumption of uniform temperature distribution at the inner surface of the 3D RPV in ABAQUS, as it is shown in Section 4.1. The physical and mechanical temperature-dependent properties of the low-alloy steel base material and the 8 mm-thick stainless steel cladding of the RPV are given in Tables 2 and 3, respectively. Additionally, a constant density of 7600 kg/m^3 , a Poisson's ratio (ν) of 0.3 and the stress-free temperature of $280 \text{ }^\circ\text{C}$ are assumed for both materials. The stress-free temperature, equal to the initial and homogeneous temperature of the RPV (see Fig. 5), assures that the initial stress state of the RPV is dominated by the pressure load only (Fig. 3). Linear elastic material properties are considered in the mechanical analyses. This is a conservative and rather realistic assumption for the irradiated RPV materials near the end-of-life, where the yield strength becomes substantially high [29].

The global model of the RPV typically requires coarser meshes than the fracture mechanics (cracked) model, where very fine meshes are placed near the crack tip. To overcome the expensive simulations of the entire structure for long transients, the sequential use of the global model and submodel is employed here. The mechanical analyses compute the displacements, strains and stresses with the global model. Then the ABAQUS submodeling technique with the eXtended FEM (XFEM) approach is used to calculate the stress intensity factor (SIF) of a postulated crack in the RPV wall. The submodeling technique interpolates the temporal displacements obtained in the global model on the submodel boundaries as mechanical boundary conditions (BC). The technique is unidirectional, so there is no feedback from the submodel to the global model. One great advantage of this technique is that only one computation of the global model is needed to analyze several crack locations, sizes and orientations with the fracture mechanics (sub-) models. Note that to ensure the submodel equilibrium, the thermo-mechanical analyses of the submodels are also required.

Fig. 7 presents a cut-view of the RPV together with the submodel, which consists of a region of the global model located directly below the cold-leg nozzle and in the middle of the core height, i.e., at the coordinate $(\theta, z) = (5, 9)$ in Fig. 2 within the cold plume and where the highest neutron embrittlement of the RPV material is expected. The colored areas of the submodel are the faces on which the boundary conditions from the global model are applied. Fig. 7 also presents the submodel mesh, which consists of 8-node bilinear bricks (C3D8) elements. The material properties of the submodel are the same as those of the global model given in Tables 2 and 3. An inner-surface, axially oriented, semielliptical crack is postulated in the RPV wall with an aspect ratio ($2c/a$) equal to 6 and depth of 10% of wall thickness ($a/th = 0.1$).

As already mentioned, the XFEM is used to calculate the SIF [13,17]. XFEM extends the classical FEM by locally enriching the solution space of the differential equations describing the fracture mechanics boundary value problem. In order to include discontinuous functions to represent the crack, the XFEM uses a displacement field approximation to model the crack face discontinuity and the near-tip asymptotic crack field [30,31]. The XFEM implementation in ABAQUS was developed for problems regarding crack propagation on non-structured, refined meshes. Previous works [13] have shown that the XFEM formulation implemented in ABAQUS for the SIF calculation may produce oscillations in the solution close to the surface points in semi-elliptical surface cracks. These oscillations depend also on the crack depth to wall thickness ratio in pipes (a/th) as discussed in Ref [32]. These two considerations have to be taken into account when applying XFEM in ABAQUS. The method provides more smooth solutions at the deepest point of the crack and, more importantly, the solutions are closer to the classical FEM and handbook solutions. Slight

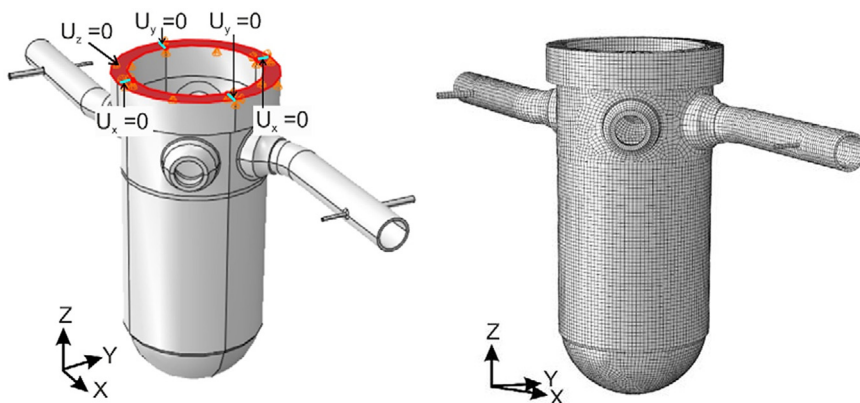


Fig. 6. Global model of the RPV. (Left) geometry and mechanical boundary conditions (u_x , u_y , u_z : displacements in x, y and z direction respectively) and (right) finite element mesh.

Table 2
Material properties of the RPV base material.

Young's Modulus E [Pa]	Expansion coef. [1/°C]	Conductivity [W/(m K)]	Specific Heat [J/(Kg K)]	Temperature [°C]
2.06E+11	1.03E−05	44.4	450	0
2.06E+11	1.03E−05	44.4	450	20
1.99E+11	1.11E−05	44.4	490	100
1.90E+11	1.21E−05	43.2	520	200
1.81E+11	1.29E−05	41.8	560	300
1.72E+11	1.35E−05	39.4	610	400

Table 3
Material properties of the stainless steel cladding.

Young's Modulus [Pa]	Expansion coef. [1/°C]	Conductivity [W/(m K)]	Specific Heat [J/(Kg K)]	Temperature [°C]
2.00E+11	1.60E−05	15.89	500	0
2.00E+11	1.60E−05	15.89	500	20
1.94E+11	1.60E−05	16.89	500	100
1.86E+11	1.70E−05	17.89	540	200
1.79E+11	1.70E−05	19.89	540	300
1.72E+11	1.70E−05	21.89	590	400

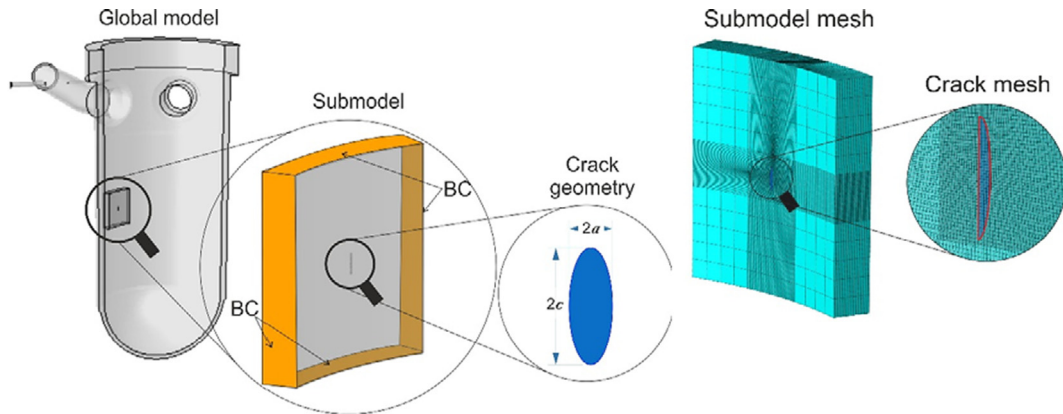


Fig. 7. Global model and submodel definition with boundary condition (BC). Inner-surface, axially oriented, semielliptical crack geometry description within the submodel (a : crack depth and $2c$: crack length).

refinement of the mesh around the crack has been applied to alleviate the SIF oscillations. The main consequence of the formulation is that it is not necessary to adapt the mesh to include the crack. The submodel consists then of XFEM approximation in the crack domain and standard finite elements in the remaining. The enrichment with additional degrees of freedom is associated with the nodes of the element affected by the crack [33] and it is given by:

$$\mathbf{u}_{XFEM}(\mathbf{x}) = \sum_{i \in C} \underbrace{N_i(\mathbf{x})}_{\text{Classical}} \mathbf{u}_i + \sum_{i \in D} \underbrace{N_i(\mathbf{x})}_{\text{Discontinuity}} H(\mathbf{x}) \mathbf{a}_i + \sum_{i \in S} \underbrace{N_i(\mathbf{x})}_{\text{Enriched}} \left[\sum_{\alpha=1}^4 \underbrace{F_{i\alpha}(\mathbf{x})}_{\text{Singularity}} \mathbf{b}_{i\alpha} \right] \quad (1)$$

where C is the set of all nodes in the mesh, $N_i(\mathbf{x})$ are the nodal shape functions and \mathbf{u}_i stand for the physical nodal displacement for non-enriched nodes at node i . The sets D and S contain the nodes enriched with the Generalized Heaviside function $H(\mathbf{x})$ and the crack tip functions $F_{i\alpha}(\mathbf{x})$, respectively, with \mathbf{a}_i and $\mathbf{b}_{i\alpha}$ being the corresponding degrees of freedom.

In ABAQUS, the interaction integral is used to obtain the stress intensity factor in mixed mode problems. This method, introduced by Shih et al. [34,35], is based on the J -integral. The SIFs are calculated as

$$\mathbf{K} = 4\pi \mathbf{B} \cdot \mathbf{J}_{\text{int}}^{\alpha} \quad (2)$$

where \mathbf{K} is the vector of stress intensity factors, $\mathbf{B} = \text{Diag}[E', E', 2G]$ is the pre-logarithmic energy factor matrix with $E' = E/2(1 + \nu)$ and G the shear modulus and the interaction energy integral is defined as [25],

$$J_{\text{int}}^{\alpha} = \lim_{\Gamma \rightarrow 0} \int_{\Gamma} \mathbf{n} \cdot \mathbf{M}^{\alpha} \cdot \mathbf{q} d\Gamma, \quad (3)$$

where Γ stands for a contour that lies in the normal plane at given position along the crack front, beginning on the bottom surface of the crack and ending on the top surface. \mathbf{n} is the outward normal to the area of the small tubular surface enclosing the crack tip given by $dA = dsd\Gamma$ and \mathbf{q} is the local direction of the virtual crack propagation. \mathbf{M}^{α} stands for the Eshelby's momentum tensor in terms of the auxiliary displacement, strain and stress fields and is given by

$$\mathbf{M}^{\alpha} = \boldsymbol{\sigma} : \boldsymbol{\varepsilon}_{\text{aux}}^{\alpha} : \mathbf{I} - \boldsymbol{\sigma} \cdot \left(\frac{\partial \mathbf{u}}{\partial \mathbf{x}} \right)_{\text{aux}}^{\alpha} - \boldsymbol{\sigma}_{\text{aux}}^{\alpha} \cdot \frac{\partial \mathbf{u}}{\partial \mathbf{x}} \quad (4)$$

where $\boldsymbol{\sigma}$ and $\boldsymbol{\sigma}_{\text{aux}}^{\alpha}$ are the stress and auxiliary stress tensors, $\boldsymbol{\varepsilon}_{\text{aux}}^{\alpha}$ is the auxiliary strain tensor and \mathbf{I} stands for the second order identity tensor. The mixed-mode stress intensity factors can be extracted from Eq. (2) through appropriate definition of the auxiliary fields, typically selected to be a Williams series for a straight crack [36,37]. The calculation of the line integral in Eq. (3) in ABAQUS follows the domain integral procedure. For this, an interaction integral for a virtual crack advance $\lambda(s)$ is defined as:

$$\bar{J}_{\text{int}}^{\alpha} = \int_L J_{\text{int}}^{\alpha}(s) \lambda(s) ds = \int_A \lambda(s) \mathbf{n} \cdot \mathbf{M}^{\alpha} \cdot \mathbf{q} dA, \quad (5)$$

where dA is a surface element on a vanishingly small tubular surface enclosing the crack tip (i.e. $dA = dsd\Gamma$). Applying the divergence theorem of Gauss in the last term of the equality in Eq. (5) and discretizing $\lambda(s)$ with the same interpolation function used in the finite elements along the crack front, the interaction integral value J_{int}^{α} is calculated at each node set P along the crack front line as [25]

$$J_{\text{int}}^{\alpha, P} = \bar{J}_{\text{int}}^{\alpha, P} / \int_L N^P ds. \quad (6)$$

The global model and submodel are used in this paper to perform the integrity analyses of the RPV and to evaluate the likelihood of crack propagation during the loss of coolant accidents leading to PTS events. The analyses are based on the comparison of K_I with the fracture toughness of the RPV base material (K_{Ic}), which is calculated according to the American Society of Mechanical Engineers (ASME) code [38,39] for every temperature (T):

$$K_{Ic} = 36.5 + 22.78 \exp[8.036(T - RT_{NDT})] \quad (7)$$

The neutron irradiation effect is considered in the value of the ductile-to-brittle (Nil ductility) transition temperature, RT_{NDT} . In the analyses presented in this paper, RT_{NDT} is set to 93 °C, which is the Swiss regulatory limit for the operation of nuclear power plants.

3.2. One-dimensional analyses of the RPV: code, model and assumptions

The FAVOR ‘‘Fracture Analysis of Vessels: Oak Bridge’’ code [24] is a dedicated code for deterministic and probabilistic integrity analyses of RPV under PTS transients. FAVOR employs an axisymmetric and 1D description of the RPV wall in the radial (wall thickness) direction. This means that the RPV is assumed to be a cylinder of infinite-length, free to expand in the axial direction and where the temperature gradients occur only in the wall thickness direction, therefore a 1D (heat diffusion) problem. The deterministic (FAVload) module of the FAVOR code is used to perform the 1D thermo-mechanical and linear-elastic fracture mechanics analyses. The temperature-dependent material properties of the 3D model of the RPV described in Section 3.1 (Tables 2 and 3) are also used in the FAVOR calculations.

As a 1D code, FAVOR requires only 1 point input data. This is the fluid pressure, temperature and the heat transfer coefficient histories during the studied transient at the location of interest. However, we are using instead the wall surface temperature histories in Fig. 5 as input. Thus, an infinite ($10^6 \text{ W/m}^2\text{K}$) heat transfer coefficient is employed, which effectively imposes the fluid temperature as the surface temperature during the heat transfer analyses in FAVOR. As in the 3D analyses, the fluid pressures shown in Fig. 3 are also used in FAVOR for the mechanical analyses. Adiabatic boundary conditions are assumed at the outer RPV surface.

The weight function method is implemented in FAVOR for the calculation of the SIF [40]. For a known weight function of the cracked component, the SIF can be obtained by multiplying this function by the stress distribution and integrating it along the crack length. In FAVOR, the SIF of an inner-surface crack is computed as:

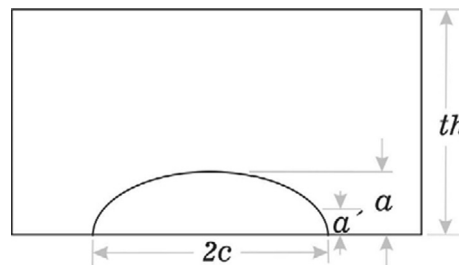


Fig. 8. FAVOR semi-elliptical surface flaw with aspect ratio $2c/a$ (th : wall thickness, a : crack depth, a' : current depth at which stress is evaluated, $2c$: crack length).

$$K_I(a) = \sum_{j=0}^3 C_j K_j^*(a) \sqrt{\pi a}, \quad (8)$$

where the coefficients C_j are obtained from a 3rd order polynomial fit to the stress distribution in the uncracked structure:

$$\sigma_n(a') = \sum_{j=0}^3 C_j (a'/a)^j, \quad (9)$$

with the stress $\sigma_n(a')$ being normal to the crack plane at the radial position a' . The variables a (crack depth) and a' are represented in Fig. 8. The coefficients $K_j^*(a)$ are the influence coefficient calibrated by FEM simulations for the normalized stress distributions (from uniform to cubic loads). The FAVOR code analyzes several crack types and sizes simultaneously. In this study, the focus is placed on the semi-elliptical, axially oriented, inner surface crack considered also in ABAQUS ($2c/a = 6$ and $a/th = 0.1$).

After the computation of the SIF, the integrity analyses proceed by comparing it to the fracture toughness of the material, Eq. (7), as explained at the end of Section 3.1.

4. Results of the RPV integrity analyses under PTS loads

This section presents the integrity analyses of the RPV under PTS loads induced by the loss of coolant accidents simulated with TRACE-3D described in Section 2. The results from the heat transfer (wall temperatures), mechanical (wall stresses) and fracture mechanics (crack SIFs) analyses performed with the 3D (ABAQUS) and 1D (FAVOR) approaches are given and compared. The 3D analyses are performed assuming both, uniform and non-uniform, temperature distributions of the RPV inner surface.

4.1. Uniform temperature distribution of the RPV inner surface

The reasons to perform the analyses assuming a uniform temperature of the RPV inner surface are twofold. First, a verification of the 3D analyses is performed with the FAVOR results. To this end, the uniform temperature of the inner surface of the 3D RPV model is imposed to reproduce, to the extent possible, the FAVOR assumptions of axisymmetric and 1D heat diffusion in the RPV wall thickness. Second, the analyses with uniform temperature should allow understanding the effects of the complex RPV geometry on the results of the 3D analyses, as compared to the cylindrical assumption in FAVOR.

In this section, the TRACE output for the LBLOCA transient at the location of interest, i.e. pressure and temperature histories given in Figs. 3 and 5, respectively, for LBLOCA are employed in both, FAVOR (1D) and ABAQUS (3D), analyses.

Fig. 9 shows the temperature and hoop stress histories at the inner surface (ri), crack tip (ct) and the outer surface (ro) of the RPV wall. Here the “crack tip stress” corresponds to the stress history at the crack tip location in the uncracked RPV, illustrating the stress at that position in the global model during the transient. Note also that the surface temperature is the common input to both simulations and has been included here for completeness. The temperatures at the crack tip and at the outer surface in Fig. 9-left show almost no differences between FAVOR and ABAQUS. The largest difference of about 60 MPa is however observed between the FAVOR and ABAQUS stresses at the inner surface at time 1.95 min into the transient.

In Fig. 10, the temperature and hoop stress profiles through-thickness are shown for selected times during the transient. The sudden change in the curves' slopes represent the boundary between the stainless steel cladding and the low alloy RPV steel. A good agreement is again obtained between the FAVOR and ABAQUS profiles. Nevertheless, the FAVOR stresses at the surface ($r/th = 0$) are systematically higher than in ABAQUS. This is correlated with the slightly higher temperature profiles from FAVOR, which could be representative of a slower heat diffusion than in ABAQUS. Thus, the larger temperature gradients through-thickness in FAVOR can explain, at least partially, the larger stresses at the more constrained surface as this cannot freely contract due to warmer neighboring regions.

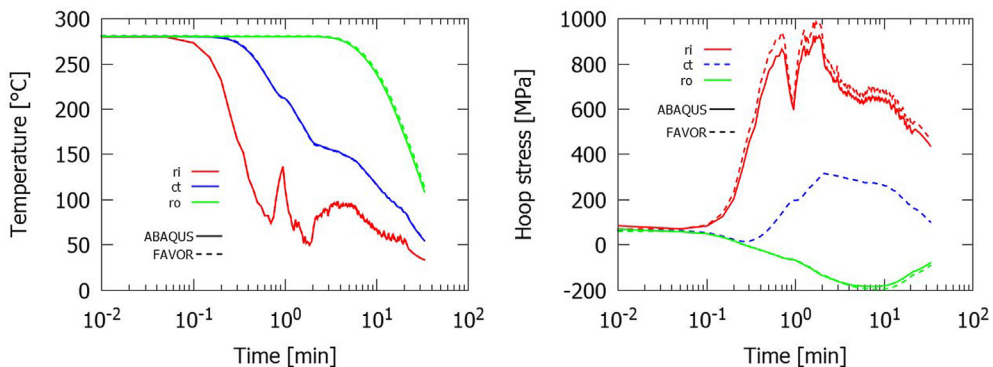


Fig. 9. Comparison of (left) temperature and (right) hoop stress histories at the inner surface (ri), crack tip (ct) and outer surface (ro) between FAVOR and ABAQUS at the RPV coordinate $(\theta - z) = (5, 9)$ during LBLOCA.

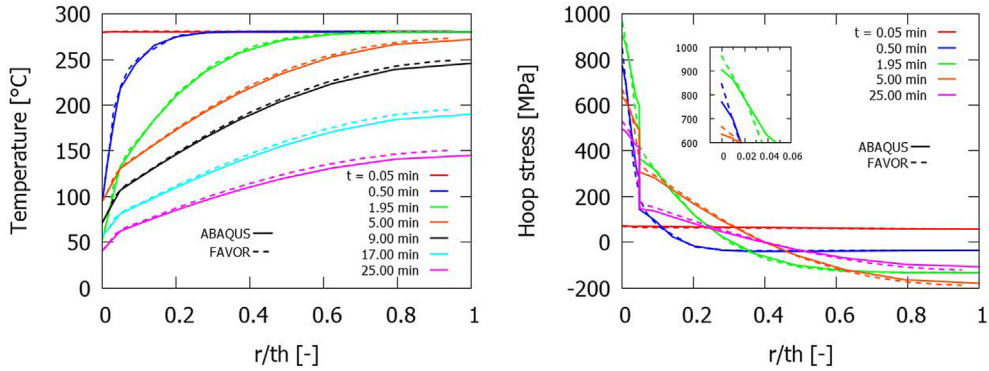


Fig. 10. Comparison of (left) temperature and (right) hoop stress profiles through normalized thickness (r/th) between FAVOR (dashed lines) and ABAQUS (full lines) at selected times and at the RPV coordinate $(\theta - z) = (5, 9)$ during LBLOCA.

Additionally, it is also of interest to investigate how the detailed RPV geometry considered in the ABAQUS model alters the stress field. Fig. 11 shows the circumferential distribution of hoop stresses at the beginning of the transient (only pressure load) and at 1.95 min into the transient (only thermal loads) at three locations along the RPV axis. Fig. 11 confirms that the presence of nozzles in the ABAQUS model causes a non-uniform distribution of the hoop stress under uniform temperature and pressure. This is compared with the FAVOR results, which, due to the axisymmetric and non-geometric details assumptions, are uniform in all directions. At time 0, the stress distribution in ABAQUS has an oval shape at the axial location of interest ($z = 9$), bringing higher stresses at $\theta = 5$ (210°) than in FAVOR. On the other hand, at $t = 1.95$ min under thermal loads only, the FAVOR stresses are clearly higher than in ABAQUS, which could be explained by the higher temperature gradient through-thickness in FAVOR observed in Fig. 10-left.

The next step in the integrity analyses is the calculation of the mode I SIF (K_I) to ultimately compare it with the fracture toughness (K_{IC}) of the RPV material given by Eq. (7). Fig. 12-left compares the stress intensity factor histories at the deepest point of the semielliptical crack obtained with ABAQUS and FAVOR. A maximum SIF with effectively the same magnitude is obtained with both codes approximately at $t = 1.95$ min. Before this maximum, the ABAQUS SIF is predominantly higher than with FAVOR, which could be explained initially by the presence of fluid pressure and the geometry (nozzle) effects. After the maximum SIF is reached, this behavior is reversed and the SIF with FAVOR is higher than with ABAQUS due to the larger stresses and thermal gradients in the former. In Fig. 12-right, the SIF versus crack tip temperature curves from both codes are compared with the fracture toughness. It can be seen that the FAVOR curve becomes higher than toughness at about 110°C and $75\text{ MPa} \cdot \text{m}^{0.5}$, which means that the postulated crack could potentially initiate a brittle growth, assuming that the material would reach the limiting RT_{NDT} of 93°C and warm pre-stress effects are ignored [41,42]. Although not far from the FAVOR results, the ABAQUS curve does not become higher than fracture toughness, meaning that the postulated crack would potentially remain at rest.

The comparison of the analyses results with ABAQUS and FAVOR has shown rather small differences between the codes regardless of the obvious different assumptions and calculation approaches. Nevertheless, such small differences in the results could have significant consequences in the RPV integrity analysis.

It can be inferred from the results in Figs. 10–12 that the differences between the 1D and 3D analyses can be also expected, to

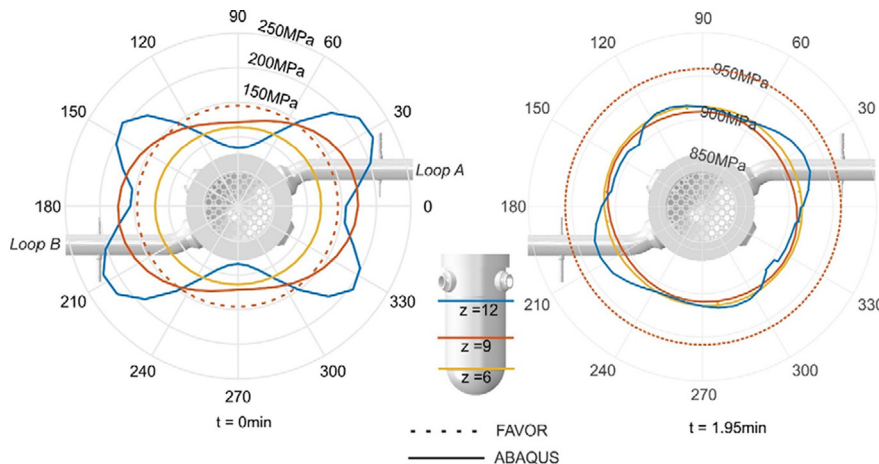


Fig. 11. Surface hoop stresses at three axial locations for uniform RPV inner surface temperature: (left) at $t = 0$ min with only pressure load and (right) at $t = 1.95$ min with only thermal load (see pressure history for LBLOCA in Fig. 3). The RPV upper view is superimposed to show that the maximum stresses in ABAQUS appear below the nozzles.

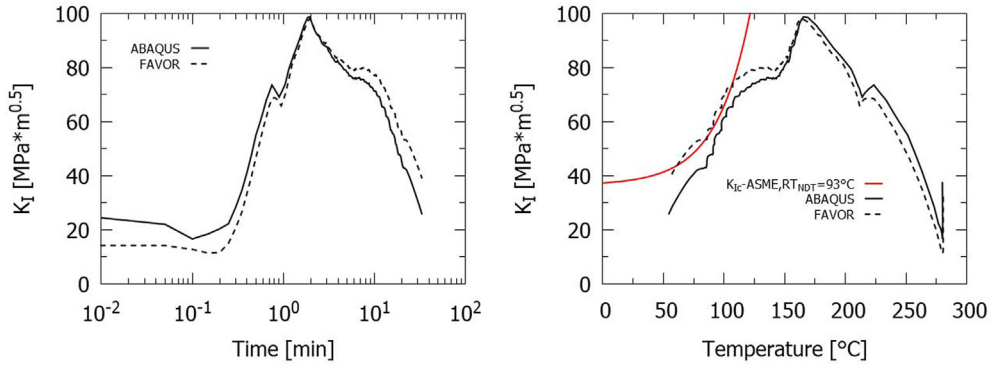


Fig. 12. Mode I SIF (K_I) at the deepest point of the semielliptical inner-surface axial crack during LBLOCA. Comparison between FAVOR and ABAQUS results. (Left) K_I history and (right) K_I versus crack tip temperature against fracture toughness (K_{Ic}).

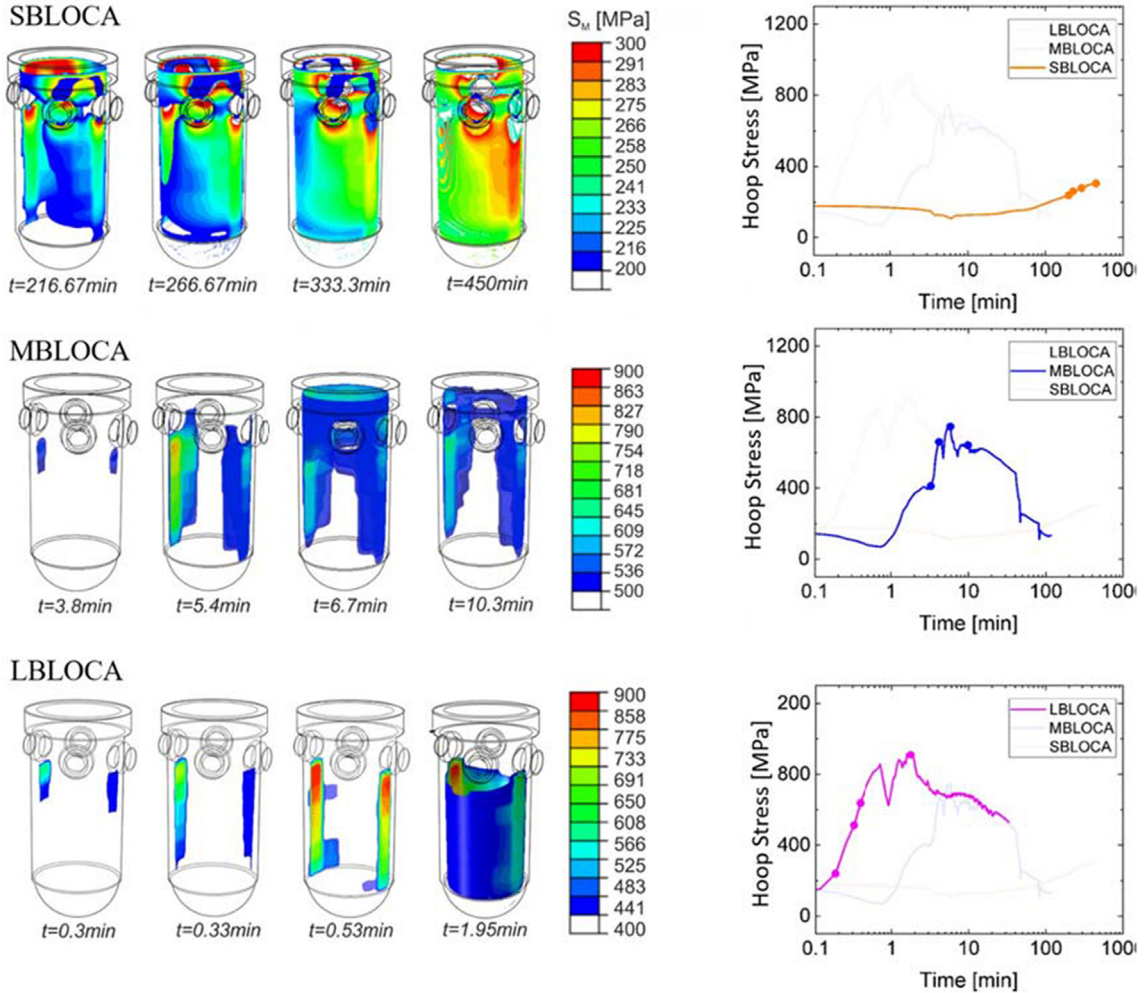


Fig. 13. (Left) von Mises stress (S_M) distribution in the RPV wall region of the cooling plume for different times and (right) hoop stress histories at the inner surface with RPV coordinates $(\theta - z) = (5, 9)$, during SB-, MB- and LBLOCA transients.

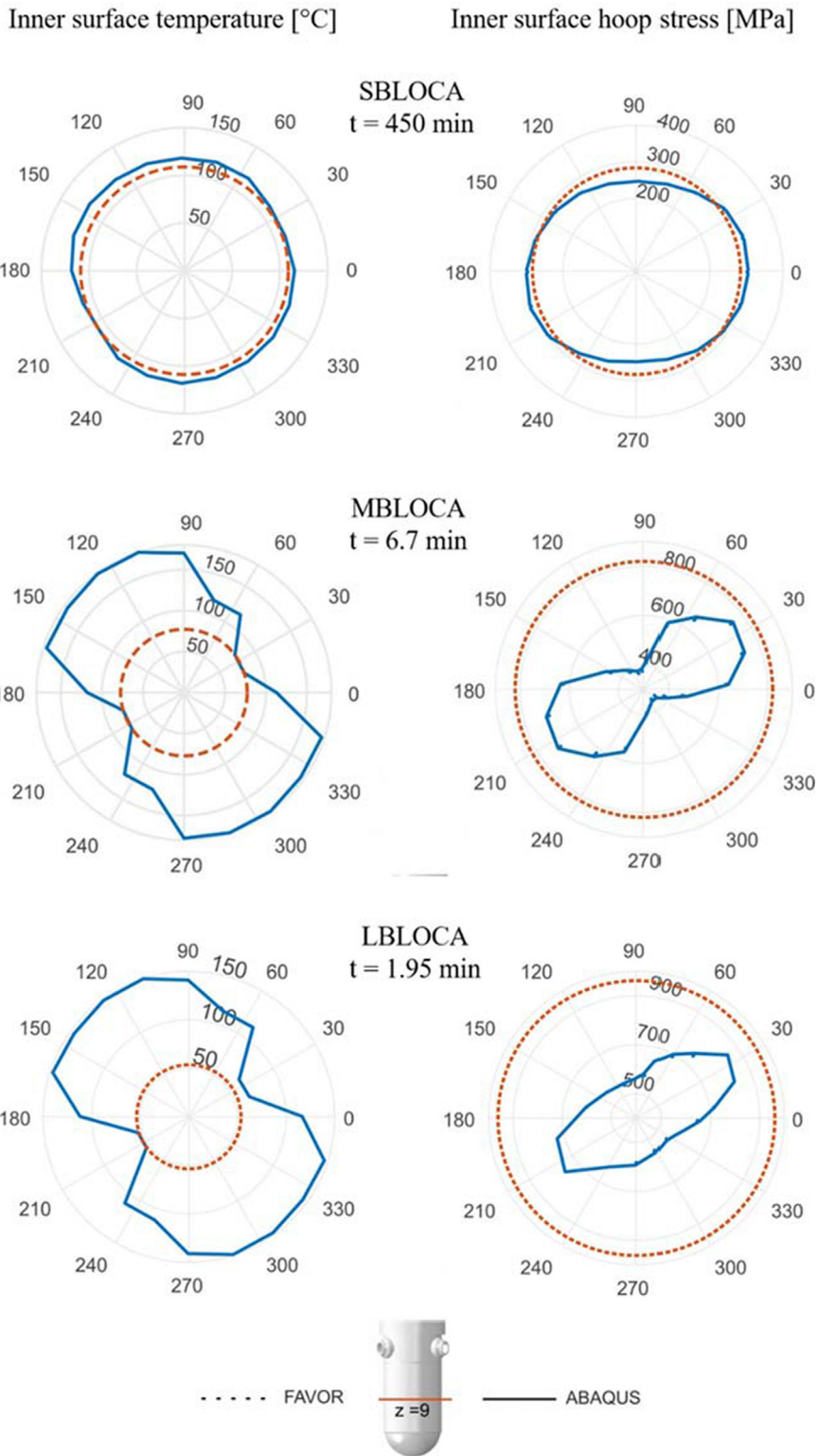


Fig. 14. Circumferential distribution of inner wall surface temperatures (left) and hoop stresses (right) at the middle of the core height and at selected times for the three transients. Note that the concentric circles in the left and right figures represent, respectively, temperature and stress levels.

some extent, in the following analyses with non-uniform temperature of the RPV inner surface due to the presence of the cold water plume.

4.2. Non-uniform temperature distribution of the RPV inner surface

In this section, the 3D and time-dependent temperatures from TRACE of the RPV inner surface for the three transients considered (see Fig. 4) are used in the analyses together with the fluid pressure histories in Fig. 3. The results of the 3D analyses with ABAQUS are compared with the FAVOR results also in this section for the sake of reference. Note that the FAVOR results for the LBLOCA case are the same as those shown in Section 4.1.

Fig. 13-left shows the von Mises stress (S_M) distributions at different times as obtained by ABAQUS for the SB-, MB- and LBLOCA transients. The stress patterns given by the distributions resemble, to a great extent, the inner wall surface temperatures in Fig. 4. This behavior, discussed already in Mora et al. [17], basically means that the high stress regions during a PTS are localized at the cold plume from the ECC water injection. The hoop stress histories in Fig. 13-right correspond to the location of interest with RPV coordinate $(\theta - z) = (5, 9)$ in Fig. 2, i.e., the inner surface point at the middle of the core height, subjected to intensive irradiation, and within the cold plume. The dots in the stress history curves mark the times at which the respective distributions in the left-hand side are displayed.

It can be seen in Fig. 13 that the stresses, representative of the cold plumes below the nozzles (30° and 210° in Fig. 2), develop at different times depending on the break size and, therefore, on the ECC flow rate. The distribution of the stresses for SBLOCA depicts the maximum stress close to the nozzle appearing at about 200 min after the beginning of the injection. For MBLOCA, the cooling plume starts earlier, at around 3.5 min, after the beginning of the accident. This earlier development can be explained due to the higher ECC water flow rate, which cools down the inner wall faster than in the small break. The region of high stresses for MBLOCA covers a broader area of the RPV inner surface with predominant concentration below the nozzles. For the LBLOCA transient, the region of high stresses is again below the nozzles but clearly more localized. In this case, the cooling plume starts to form at about 20 s after the beginning of the transient.

Fig. 14 shows, for the three transients considered, the inner surface temperature and hoop stress distributions at the middle of the core height ($z = 9$) and at selected times near the hoop stress maxima. The results from ABAQUS and FAVOR are again compared. One more time, this figure emphasizes the location of the cooling plumes with lower temperatures and higher stresses below the nozzles (30° and 210°), which are clearly more localized for the large and medium breaks than for the small break. Recall that the FAVOR analyses employ the inner surface temperature histories at $(\theta - z) = (5 \text{ or } 210^\circ, 9)$ as input. The FAVOR stresses are higher than in ABAQUS for the MB- and LBLOCA transients due to larger thermal gradients through-thickness in the former (see the explanation of Fig. 10). However, this is not necessarily the case in SBLOCA where the remaining system pressure (Fig. 3) combined with the nozzle geometry may keep the ABAQUS stresses higher than in FAVOR in certain locations, as it was explained in Fig. 11.

The stress intensity factor histories at the deepest point of the semielliptical crack obtained with ABAQUS and FAVOR and for the three transients are shown in Fig. 15-left. Similar trends as for the uniform case in Fig. 12 are also observed here for non-uniform temperature distribution. At the beginning of the transients, the SIF with ABAQUS are higher than with FAVOR. This can be explained initially due to the combination of pressure and nozzle effects. This behavior is however extended along the entire duration of the SBLOCA transient due to the remaining system pressure. Thus, for transients originating from relatively small break sizes such as the SBLOCA, the FAVOR SIFs may be underestimated due to the missing nozzle geometry in combination with the system pressure. The SIF maxima for MB- and LBLOCA are also here very similar, with a time-shift of the former explained by the delayed ECC water injection (Fig. 5). It can be seen also in Fig. 15-left that the SIF curve for SBLOCA is kept at relatively low values due to the slower temperature gradient of this transient, as shown in Fig. 5, which effectively induces lower thermal stresses and, thus, lower SIF

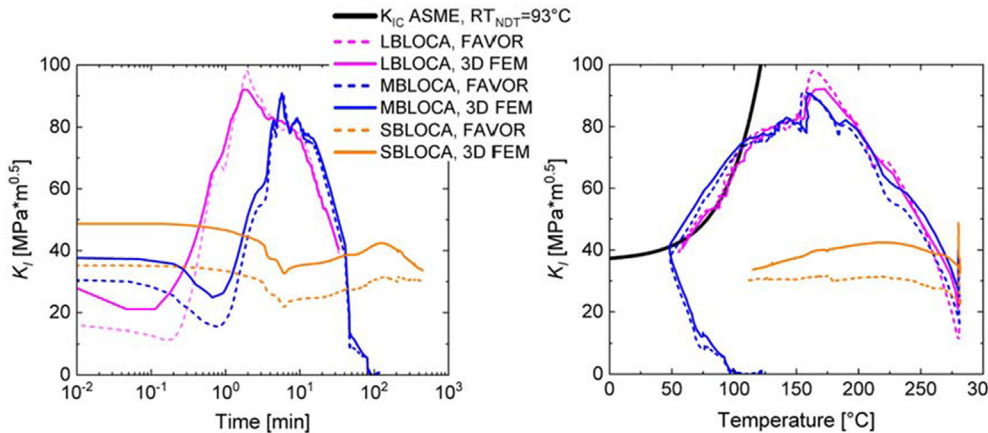


Fig. 15. Mode I SIF (K_I) at the deepest point of the semielliptical surface axial crack. Comparison between FAVOR and ABAQUS (3D FEM) results for the three transients considered. (Left) K_I history and (right) K_I versus crack tip temperature against fracture toughness (K_{Ic}).

(Figs. 13 and 14).

Fig. 15-right depicts the SIF versus crack tip temperature curves also for the three transients obtained with both codes and these are compared with the fracture toughness. The SIF curves for MB- and LBLOCA using both codes can be seen to cross the fracture toughness while descending from their maximum values. Thus, if the warm pre-stress concept is not accepted in an integrity assessment, brittle crack propagation would be considered likely during these two transients [41,42]. As compared to the uniform case in Fig. 12, the ABAQUS curve for LBLOCA is now seen to follow more closely the FAVOR curve towards the end of the transient and, therefore, crossing the toughness curve. This can be ascribed to the presence, with non-uniform temperature, of warmer regions outside of the cold plume, which additionally preclude the crack location from contracting freely and, thus, higher values of SIF keeping the crack open. The SIF in the SBLOCA case is, nevertheless, far below the fracture toughness. Clearly, this transient is not relevant to RPV safe operation, according to the present analysis.

Fig. 16 illustrates the evolution of the stress intensity factor accompanied by the distribution of the temperature at different times of the LBLOCA transient. It can be seen that at the peak of the curve (around 104 s) the cooling plume is visible. After that, the plume remains below the nozzle occupying mainly the column of cells in the centerline of the nozzle.

5. Conclusions

The integrity analyses of RPV under PTS loads have been performed in this paper with the one-way multi-step simulation strategy using TRACE and XFEM. The progress in the application of the strategy is illustrated with three examples of loss of coolant accidents. The comparative analysis with the well-known code FAVOR highlighted the differences between 1D and 3D models of the RPV. It has been shown that the combined effects of the geometric irregularities and thermo-mechanical loading influence the SIF values for a postulated semi-elliptical surface crack in the RPV wall. The following conclusions can be drawn:

- (1) The analysis for the LBLOCA transient with uniform temperature distribution of the inner RPV surface has been performed to replicate the FAVOR axisymmetric and 1D (radial) heat diffusion assumptions. The 3D analyses in ABAQUS have shown that the stresses are non-uniform due to the presence of the nozzles. At the beginning of the transient (only pressure), the stresses and SIF from ABAQUS are found to be higher than with FAVOR. This behavior is reversed under thermal loads only due to higher thermal gradients through-thickness in FAVOR, possibly induced by slower heat diffusion.
- (2) With non-uniform temperature distribution of the RPV inner surface, the non-uniformity of the stress fields is even more pronounced due to the presence of the cooling plumes. Regardless of the obvious different assumptions and calculation approaches, ABAQUS and FAVOR have been shown to provide very similar results for the LBLOCA and MBLOCA transients. For these transients, the SIF versus crack tip temperature curves cross the fracture toughness while descending from their maxima. If the warm pre-stress concept is accepted, it can be postulated that brittle crack propagation would not occur.
- (3) Although not necessarily relevant for the RPV integrity, transients originating from relatively small break sizes analyzed with the FAVOR code, such as the SBLOCA, could underestimate the SIFs due to the missing consideration of the nozzle geometry in combination with the system pressure.

Finally, the outcome of the analyses presented also corroborates that the use of the one-way multi-step simulation strategy with TRACE and XFEM reduces the computational costs and the number of assumptions and approximations needed for feasible and reliable 3D fracture mechanics analyses of the RPV with consideration of the cooling plume effect.

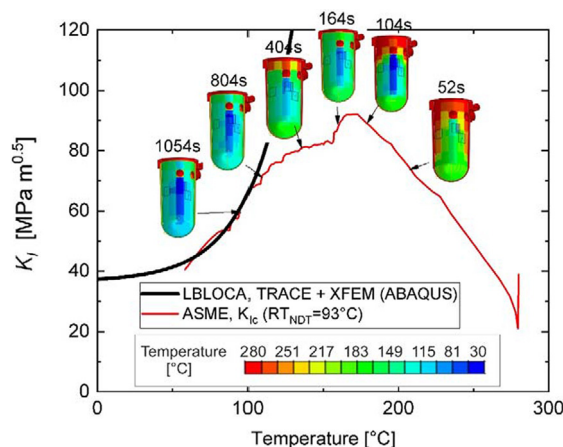


Fig. 16. Stress intensity factor at the deepest point of the semielliptical axial crack versus crack tip temperature during non-uniform cooling and compared to fracture toughness (K_{Ic}).

Declaration of Competing Interest

The authors declare that they have no known competing financial interests or personal relationships that could have appeared to influence the work reported in this paper.

Acknowledgement

The authors are grateful for the financial support of the PROBAB (Contract No. H-101247) and PROACTIV (Contract No. CTR-00489) projects provided by the Swiss Federal Nuclear Safety Inspectorate (ENSI).

References

- [1] Lucas GE. The evolution of mechanical property change in irradiated austenitic stainless steels. *J Nucl Mater* 1993;206:287–305.
- [2] Integrity of reactor pressure vessels in nuclear power plants: assessment of irradiation Embrittlement effects in reactor pressure vessel steels. Vienna: International Atomic Energy Agency; 2009.
- [3] Qian G, González-Albuixech VF, Niffenegger M. Effects of embedded cracks and residual stresses on the integrity of a reactor pressure vessel. *Eng Fail Anal* 2018;90:451–62.
- [4] Qian G, González-Albuixech VF, Niffenegger M. In-plane and out-of-plane constraint effects under pressurized thermal shocks. *Int J Solids Struct* 2014;51:1311–21.
- [5] Qian G, Niffenegger M, Sharabi M, Lafferty N. Effect of non-uniform reactor cooling on fracture and constraint of a reactor pressure vessel. *Fatigue Fract Eng Mater Struct* 2018;41:1559–75.
- [6] Sievers J, Scheuerer M, Boyd C, D'Auria F, Filo J, Haefner W, et al. Thermal-hydraulic aspects of the international comparative assessment study on reactor pressure vessels under PTS loading (RPV PTS ICAS). Nuclear Energy Agency of the OECD (NEA); 2001. p. 260–76.
- [7] Pressurized thermal shock in nuclear power plants: good practices for assessment. Vienna: International Atomic Energy Agency; 2010.
- [8] Use and development of coupled computer codes for the analysis of accidents at nuclear power plants. Vienna: International Atomic Energy Agency; 2007.
- [9] Toppila T. CFD simulation of Fortum PTS experiment. *Nucl Engng Des* 2008;238:514–21.
- [10] Petrucci A, D'Auria F. Thermal-hydraulic system codes in nuclear reactor safety and qualification procedures. *Sci Technol Nucl Install* 2008.
- [11] RELAP5-3D. RELAP5/Mod3 Code Manual, Vol: Code Structure, System Models and Solution Methods. The Thermal Hydraulics Group, Idaho; 1999.
- [12] Murray C. TRACE V5.0 Theory Manual - Volume 1: Field Equations, Solution Methods, and Physical Models. USNR Commission; 2008. p. 696.
- [13] González-Albuixech VF, Qian G, Niffenegger M. Integrity analysis of reactor pressure vessels subjected to pressurized thermal shocks by XFEM. *Nucl Eng Des* 2014;275:336–43.
- [14] Qian G, Niffenegger M. Integrity analysis of a reactor pressure vessel subjected to pressurized thermal shocks by considering constraint effect. *Eng Fract Mech* 2013;112–113:14–25.
- [15] González-Albuixech VF, Qian G, Sharabi M, Niffenegger M, Niceno B, Lafferty N. Comparison of PTS analyses of RPVs based on 3D-CFD and RELAP5. *Nucl Eng Des* 2015;291:168–78.
- [16] González-Albuixech VF, Qian G, Sharabi M, Niffenegger M, Niceno B, Lafferty N. Integrity analysis of a reactor pressure vessel subjected to a realistic pressurized thermal shock considering the cooling plume and constraint effects. *Eng Fract Mech* 2016;162:201–17.
- [17] Mora DF, Niffenegger M, Qian G, Jaros M, Niceno B. Modelling of reactor pressure vessel subjected to pressurized thermal shock using 3D-XFEM. *Nucl Eng Des* 2019;353:110237.
- [18] Apanasevich P, Coste P, Ničeno B, Heib C, Lucas D. Comparison of CFD simulations on two-phase Pressurized Thermal Shock scenarios. *Nucl Eng Des* 2014;266:112–28.
- [19] Lucas D, Bestion D, Bodèle E, Coste P, Scheuerer M, D'Auria F, et al. An overview of the pressurized thermal shock issue in the context of the NURESIM project. *Sci Technol Nucl Install* 2009:13.
- [20] Mukin R, Clifford I, Ferroukhi H, Niffenegger M. Pressurized Thermal Shock (PTS) transient scenarios screening analysis with TRACE; 2018: V06AT8A069.
- [21] Mukin R, Clifford I, Costa Garrido O, Mora DF, Niffenegger M, Niceno B, et al. Screening Analysis for Pressurized Thermal Shock (PTS) Transient Scenarios. In: 18th International Topical Meeting on Nuclear Reactor Thermal Hydraulics (NURETH-18). Portland, OR; 2019.
- [22] Mora DF, Mukin R, Costa Garrido O, Niffenegger M. Fracture mechanics analysis of a PWR Under PTS Using XFEM and Input From TRACE. ASME 2019 Pressure Vessels & Piping Conference San Antonio, Texas, USA; 2019.
- [23] Niffenegger M, Costa Garrido O, Mora DF, Qian G, Mukin R, Sharabi M, et al. Uncertainties in pressurized thermal shock analyses. ASME 2019 Pressure Vessels & Piping Conference San Antonio, Texas, USA; 2019.
- [24] Williams PT, Dickson TL, Bass BR, Klasky HB. Fracture Analysis of Vessels – Oak Ridge FAVOR, v16.1, Computer Code: Theory and Implementation of Algorithms, Methods, and Correlations. Oak Ridge, TN, USA: Oak Ridge National Laboratory; 2016.
- [25] ABAQUS. Theory Manual and User's Manual. Dassault System Simulia Corp, Providence, RI, USA; 2012.
- [26] Murray C. Overview of TRACE v5.0. In: Regulatory Information Conference slides USNRC; 2007.
- [27] Kral P. Experimental facilities for VVER thermal hydraulic research and code validation (COVERS). *Int J Nucl Energy Sci Technol* 2007;3.
- [28] Sharabi M, González-Albuixech VF, Lafferty N, Niceno B, Niffenegger M. Computational fluid dynamics study of pressurized thermal shock phenomena in the reactor pressure vessel. *Nucl Eng Des* 2016;299:136–45.
- [29] Soneda N. Irradiation Embrittlement of Reactor Pressure Vessels (RPVs) in Nuclear Power Plants; 2014.
- [30] Dufloy M. A study of the representation of cracks with level sets. *Int J Numer Meth Eng* 2007;70:1261–302.
- [31] Sukumar N, Moës N, Moran B, Belytschko T. Extended finite element method for three-dimensional crack modelling. *Int J Numer Meth Eng* 2000;48:1549–70.
- [32] Shim D-J, Uddin M, Kalyanam S, Brust F, Young B. Application of Extended Finite Element Method (XFEM) to stress intensity factor calculations. ASME 2015 Pressure Vessels and Piping Conference; 2015.
- [33] Moës N, Dolbow J, Belytschko T. A finite element method for crack growth without remeshing. *Int J Numer Meth Eng* 1999;46:131–50.
- [34] Stern M, Becker EB, Dunham RS. A contour integral computation of mixed-mode stress intensity factors. *Int J Fract* 1976;12:359–68.
- [35] Yau JF, Wang SS, Corten HT. A mixed-mode crack analysis of isotropic solids using conservation laws of elasticity. *J Appl Mech* 1980;47:335–41.
- [36] Gosz M, Moran B. An interaction energy integral method for computation of mixed-mode stress intensity factors along non-planar crack fronts in three dimensions. *Eng Fract Mech* 2002;69:299–319.
- [37] González-Albuixech VF, Giner E, Tarancón JE, Fuenmayor FJ, Gravouil A. Domain integral formulation for 3-D curved and non-planar cracks with the extended finite element method. *Comput Methods Appl Mech Eng* 2013;264:129–44.
- [38] Regulatory Guide 1.99 Rev. 2. USNR Commission; 1988.
- [39] ASME-code. ASME boiler and pressure vessel code, section III, nuclear power plants components; 1995.
- [40] Bueckner HF. A novel principle for the computation of stress intensity factors. *ZAMM*. 1970;50:529–45.
- [41] Hure J, Vaillie C, Wident P, Moineau D, Landron C, Chapuliot S, et al. Warm PreStress effect on highly irradiated reactor pressure vessel steel. *J Nucl Mater* 2015;464:281–93.
- [42] Qian G, Niffenegger M. Investigation of constraint and warm prestressing effects by means of a local approach to fracture. *Eng Fract Mech* 2015;136:26–37.